

Structure and Function of Vanadium Haloperoxidases[†]

Simone Raugei* and Paolo Carloni

International School for Advanced Studies (SISSA/ISAS) and INFN–DEMOCRITOS Modeling Center for Research In Atomistic Simulation, Via Beirut 2-4, 34014-Trieste, Italy

Received: August 30, 2005; In Final Form: September 28, 2005

A quantum mechanics/molecular mechanics study of the resting state of the vanadium dependent chloroperoxidase from fungi *Curvularia inaequalis* and of the early intermediates of the halide oxidation is reported. The investigation of different protonation states indicates that the enzyme likely consists of an anionic H_2VO_4^- vanadate moiety where one hydroxo group is in axial position. The calculations suggest that the hydrogen peroxide binding may not involve an initial protonation of the vanadate cofactor. A low free energy reactive path is found where the hydrogen peroxide directly attacks the axial hydroxo group, resulting in the formation of an hydrogen peroxide intermediate. This intermediate is promptly protonated to yield a peroxo species. The free energy barrier for the formation of the peroxo species does not depend significantly upon the protonation state of the cofactor. The most likely protonation states of the peroxo cofactor are neutral forms $\text{HVO}_2(\text{O}_2)$ with a hydroxo group either H-bonded to Ser⁴⁰² or coordinated to Arg³⁶⁰. The peroxo cofactor is also coordinated to an axial water molecule, which could be important for the stability of the peroxovanadate/His⁴⁹⁶ adduct. Our calculations strongly suggest that the halide oxidation may take place with the preliminary formation of a peroxovanadate/halogen adduct. Subsequently, the halogen reacts with the peroxo moiety yielding a hypohalogen vanadate. The most reactive protonation state of peroxovanadate is the neutral $\text{HVO}_2(\text{O}_2)$ with the hydroxo group H-bonded to Ser⁴⁰². The important role of Lys³⁵³ in determining the catalytic activity is also confirmed.

1. Introduction

Since the discovery of vanadium redox enzymes about 2 decades ago, there has been an increasing interest in the biological, pharmacological, and industrial applications of vanadium.^{1–6} Two classes of vanadium-based enzymes have so far been identified: vanadium–nitrogenases and vanadate-dependent haloperoxidases. The vanadium–nitrogenases⁷ activate and reduces several substrates such as molecular nitrogen.⁸ Vanadium–haloperoxidases (VHPOs) contain vanadium(V) as vanadate or related ions and catalyze the two-electron oxidation of a halide ion, X^- , to the hypohalous acids, HXO .⁴



HXO can further react with a wide range of activated C–H bonds under acidic conditions, generating diverse halogenated natural products, in particular in the marine biosphere.^{2,9} The names of VHPOs are assigned on the basis of the most electronegative halide they can oxidize. Thus, a vanadium chloroperoxidase is able to oxidize Cl^- , Br^- , and I^- .

Understanding the reaction mechanism of these proteins may help the design of biomimetic vanadium complexes, which have attracted considerable attention as putative oxidation and oxo transfer catalysts.^{4,6,10–16} Peroxovanadium complexes represent good functional models of the VHPO and have been shown to epoxidize alkenes,¹⁷ hydroxylate hydrocarbons,¹⁸ and oxidize many organic compounds,^{14,19} and they can perform efficient enantioselective sulfoxidations.^{20,21}

Three vanadate-dependent peroxidases have been structurally characterized so far: from brown algae (*Ascomyces nodosum*),²² from red algae (*Corallina officinalis*),²³ and from fungi (*Curvularia inaequalis*).^{24,25} For the latter, the X-ray structure of the adduct with the peroxo intermediate has also been solved.²⁴ These enzymes possess a high degree of amino acid sequence homology in the active site cavity. These structures have revealed that the vanadate moiety is bound to the N ϵ of an imidazolyl ring of a proximal histidine residue, and it is further hydrogen-bonded to a distal histidine and water molecules, giving rise to an trigonal-bipyramidal geometry (Figure 1a).

Although a large number of organic compounds are known to be halogenated by haloperoxidases, a thorough understanding of the mechanism by which this occurs is not fully understood. Upon coordination of the peroxo group, it is clear that a structural rearrangement to a tetragonal pyramid takes place²⁵ (Figure 1b). On the basis of a variety of experimental^{14,6,14,15,24–32} and theoretical^{12,33–37} studies, the following scenarios for the protonation state at the active site and reaction mechanisms have been proposed. (i) The X-ray structure of the apo form of V–ClPO is identical to the native structure, suggesting that the protein scaffold is rigid and provides a preformed cofactor binding site.²⁶ (ii) The oxidation state of the vanadium (+V) does not change during catalysis, and therefore, the metal acts as a strong Lewis acid with respect to the actual oxidant hydrogen peroxide.³ (iii) Most likely, the axial oxygen of the vanadate–histidine complex is protonated in *C. officinalis* at pH = 8.²⁴ It is however unclear whether other oxygens of the vanadate moiety are protonated. There are three possibly positively charged groups at the active site directly coordinated to the cofactor: two guanidiniums (from Arg³⁶⁰ and Arg⁴⁹⁰,

[†] Part of the special issue “Michael L. Klein Festschrift”.

* Corresponding author. E-mail: raugei@sissa.it.

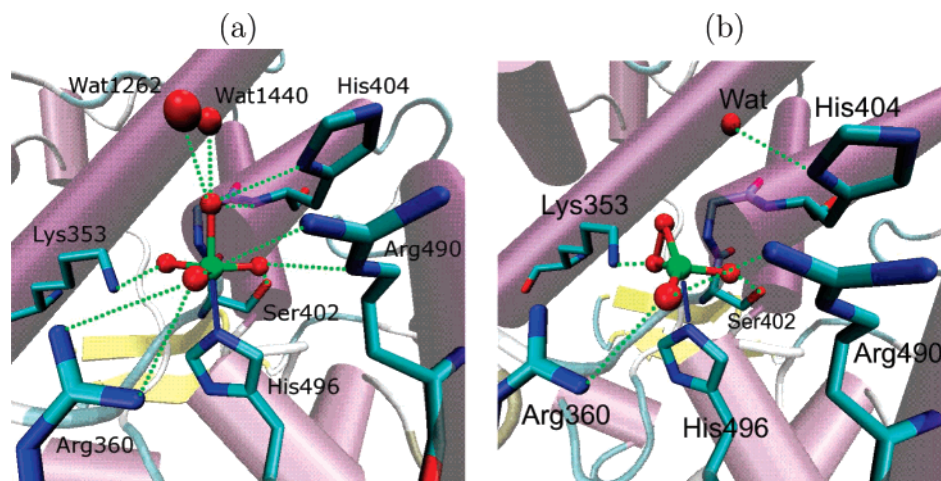


Figure 1. Crystal structure of the (a) native and the (b) peroxide form of the vanadium-containing chloroperoxidase from fungus *C. inaequalis*.²⁵ A possible hydrogen bonding pattern is drawn as dotted lines.

C. officinalis numbering) and one ammonium (from Lys³⁵³). The cofactor also forms a H-bond with a serine (Ser⁴⁰²) and with the protein backbone peptidic N–H group (Gly⁴⁰³ and Arg⁴⁹⁰, Figure 1a). Recent computational studies by Pecoraro and co-workers³⁵ of the protonation state of gas-phase models of the native VHPO indicate that the vanadate cofactor is likely in an anionic H_2VO_4^- form that along with the charges of the enzyme pocket creates a cationic (or neutral) active site. (iv) It is supposed that the hydrogen bond between the apical cofactor $\text{O}_\text{a}\text{H}$ group and His⁴⁰⁴ makes that hydroxy unit more nucleophilic.²⁵ Hence, when a hydrogen peroxide molecule approaches the active site, the apical vanadate OH^- is protonated and HOO^- is released. The weakly bound water molecule then dissociates from the cofactor and a peroxide intermediate is generated after the formation of a second water molecule. (v) The binding site of halides or organic sulfides is not clear even though there are evidences of a nucleophilic site opposite to the peroxo ligand.²⁷ It has also been proposed that the first steps of halogen oxidation may involve the protonation of the peroxo group.^{14,15} Further computational investigations on models of the peroxo-vanadium cofactor³⁶ suggest that the protonation state of Lys³⁵³ plays a fundamental role in activating the peroxo moiety for the oxo-transfer.

All of the theoretical studies^{12,33–37} on VHPO performed so far are based on simple models of the active site in vacuo. Although they provide an important piece of information, it has been proposed, however, that the role of the protein environment via supramolecular interactions²⁸ could be crucial in determining the stability of the active site. Moreover, a detailed analysis of the mechanism of formation of the peroxo intermediate and the early stages of halogen oxidation at finite temperature is still lacking.

Herein we focused on vanadium chloroperoxidase from *C. inaequalis*. We employed *ab initio* (Car–Parrinello)-molecular mechanics (CP/MM) simulations^{38–40} (section 2) to clarify the structure of the vanadate cofactor and the reactivity vs hydrogen peroxide and bromide anion. The study was performed taking fully into account the field of the entire protein, solvent and counterions. We found that at physiological conditions the vanadate moiety is likely present as dioxovanadium(V), VO_2^+ coordinated to two hydroxyl anions, giving formally rise to a H_2VO_4^- anion (section 3.1). In addition, the peroxovanadate species, which likely proceeds through a hydrogen peroxide intermediate (section 3.2), is in a monoprotonated neutral state with a water molecule coordinated in the axial position (section 3.3). The peroxo cofactor forms an adduct with the halogen,

which in turn readily reacts yielding an hypohalogen vanadate species (section 3.4).

2. Computational Details

The study was carried out in two distinct stages. In the first stage, classical molecular dynamics (section 2.1) was used to equilibrate the vanadium haloperoxidase for *C. inaequalis*²⁴ in aqueous solution. Then, hybrid QM/MM simulations (section 2.2) were performed to determine the protonation state of the active site in order to study the binding of hydrogen peroxide and, subsequently, of the bromide anion (see section 2.3).

2.1. Classical Molecular Dynamics. The water solvated crystal structure of the resting state of the enzyme²⁴ (protein data bank, pdb,⁴¹ entry: 1IDQ) and of the peroxo form²⁴ (pdb entry: 1IDU) were relaxed in aqueous solution using classical molecular dynamics. If not otherwise stated, aspartates and glutammates were taken in the anionic form, whereas lysines and arginines were considered to be positively charged. His⁴⁰⁴ was considered to be either charged or neutral (protonated at N_δ). Several protomers differing for number and location of the protons were considered (see model a to model p, Figures 2 and 7). The systems were enclosed in a orthorhombic cell and solvated by about 20 000 water molecules with additional Na^+ counterions to ensure neutrality.

The Amber⁴² force field was used for the protein, water, and counterions. Atom–atom parameters for vanadate and peroxo-vanadate cofactors were taken according to ref 43, whereas atomic point charges were calculated using the RESP scheme adopted in Amber for the imidazole/vanadate and imidazole/peroxo cofactor complexes. Charges for different protonation states were calculated. During these simulations both the cofactor and His⁴⁹⁶ were constrained to the crystallographic positions. The electrostatic interactions were treated using a particle mesh Ewald summation. For each protonation state studied, equilibration was achieved by a 500 ps restrained molecular dynamics in which a harmonic potential of 20 kcal mol^{−1} Å^{−2} was applied to each atom. During the simulations the restraining potential was gradually switched off, thus allowing the protein structure to slowly adjust to the presence of the solvent and counterions. At the same time, the temperature was raised from 0 to 300 K using a stochastic rescaling of the atomic velocities and allowing the cell to readjust its volume. Next, the system was equilibrated for a further 0.8–1.0 ns, depending on the protonation state of the catalytic pocket, controlling the temperature with a stochastic (Berendsen)

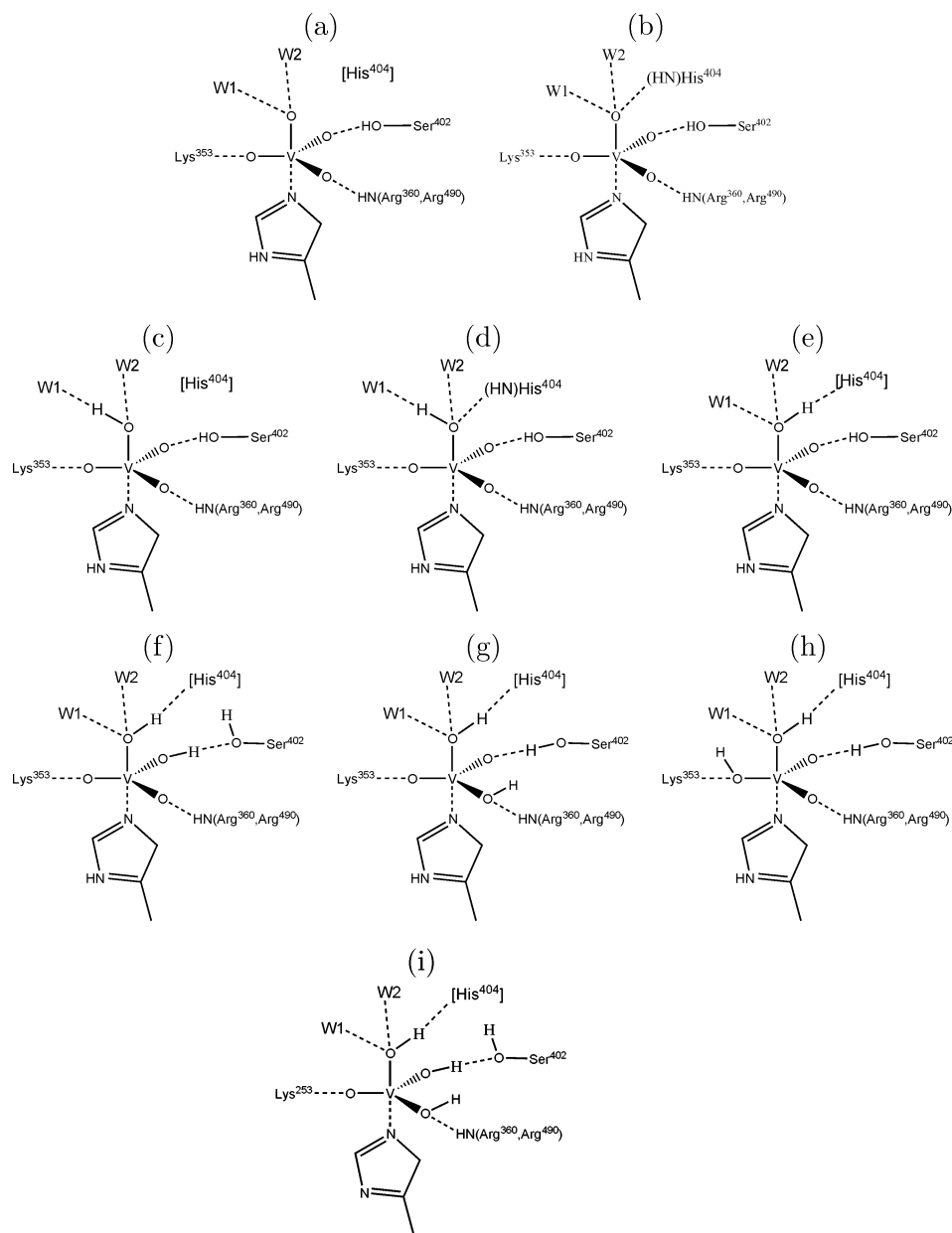


Figure 2. Vanadate protonation states and H-bonding patterns examined. The residues that are explicitly taken into account at the quantum level of theory are reported. His⁴⁰⁴ is indicated in square brackets for the simulations where it is not included in the quantum subsystem.

thermostat of frequency 1 ps^{-1} . Finally, in all of the simulations the density fluctuations were controlled by a stochastic (Berendsen) barostat of frequency 1 ps^{-1} .

2.2. Hybrid Car—Parrinello/Molecular Mechanics Simulations. The final MD structures were partitioned into two parts.⁴⁴ The active site (the cofactor and His⁴⁹⁶, His⁴⁰⁴, Arg³⁶⁰, Arg⁴⁹⁰, Lys³⁵³, Ser⁴⁰²) was treated at the quantum level, whereas the rest of the system was treated with the Amber force field.⁴² When present, water, hydrogen peroxide, and bromide anion were included in the QM region. The covalent links between the QM and the MM regions were treated with a capping procedure whereby hydrogens are added to saturate the valence of the boundary QM atoms.⁴⁴ The two histidines were modeled as imidazolyl fragments, the arginines as guanidinium cations, the lysine as methylamine, and, finally, the serine as methanol. Different protonation states of the Lys³⁵³, Arg³⁶⁰, Arg⁴⁹⁰, and Lys³⁵³ were considered as discussed in sections 3.1 and 3.3. The electrostatic coupling between the QM and the MM region was calculated using the fully Hamiltonian scheme proposed by Rothlisberger and co-workers^{39,40} as implemented in the

Car—Parrinello code CPMD3.9.⁴⁵ Briefly, the MM subsystem is split in three regions centered around the QM part. The inner region consists of enzyme residues within 7 \AA of the QM part, and the electrostatic interaction energy between this region and the QM area is directly computed using the QM charge density and the MM point charges.³⁹ To avoid an unphysical charge escape from the QM region (the so-called spill-out problem) a short-range modified Coulomb interaction was used³⁹ to mimic Pauli repulsion at each MM atom site. The second region consists of all the residues between 7 and 18 \AA . The electrostatic interaction between the QM and this MM region is calculated as a point charge—point charge interaction, where the charges associated with the QM part are calculated on-the-fly using the RESP scheme proposed by Laio et al.⁴⁰ Finally, the electrostatic interaction between the third region, which is composed by all the remaining MM atoms, and the QM region is computed by a multipolar expansion of the QM charge density up to the quadrupole term.³⁹

The quantum region was described within gradient-corrected DFT using the HCTH exchange-correlation functional,⁴⁶ which

TABLE 1: Imidazole N–Vanadium Distance, d (Å), and Relative Energies, ΔE (kJ mol^{−1}), of Different Di- and Triprotonated Vanadate/Imidazole Complexes^a

model	method	$d(\text{V}-\text{N})$	ΔE
a, e	HCTH	2.201	
	B3LYP	2.279	
	MP2	2.219	
a, e, e	HCTH	2.159	0
	B3LYP	2.226	0
	MP2	2.208	0
e, e, e	HCTH	2.201	32.1
	B3LYP	2.398	16.3
	MP2	2.249	42.9

^a “a” and “e” stand for axial and equatorial oxydriol groups, respectively.

has been demonstrated to give good energy barriers,^{46–49} especially for proton transfers.^{46,49} Norm-conserving Martins–Troullier pseudo-potentials⁵⁰ were used to describe the interactions between the core and valence electrons for all atoms except for hydrogen, where a Von Bart–Car-type pseudopotential was employed to smooth out the divergence in the Coulombic potential at the nucleus.⁵¹ The Kohn–Sham orbitals of valence electrons were expanded in plane waves with kinetic energy up to 70 Ry. For the Car–Parrinello dynamics,³⁸ a fictitious electronic mass of 400 au was used, which allowed an integration of the equations of motion with a time step of 0.097 fs. The CP/MM simulations were started from an equilibrated structure obtained by classical MD. The positions of atoms in the QM region were optimized. Then the system was reequilibrated for 1 ps at 300 K in the *NVT* ensemble and the configurational space was sampled for further 4–5 ps.

The reliability of the use of the HCTH functional was verified by comparing HCTH/PW calculations to MP2 and B3LYP calculations with localized basis sets on vanadate/imidazole complexes in vacuo.⁵² For the latter, the 6-311++G(d,p) basis set was used for all of the atoms except vanadium for which the LAND2DZ along with an effective core potential was employed. These calculations indicate that only the di- and triprotonated vanadate/imidazole complexes are stable, consistently with previous studies.³⁵ For the diprotonated complex, only the protomer with an axial oxydriol group is stable. As a gauge for the performance of this approach in this particular system, the imidazole N–vanadium distance and relative energy of different stable protomers are reported in Table 1, which indicate a maximum error of ≈ 0.018 Å in V–N bond length and only ≈ 10 kJ/mol in relative energy with respect to MP2.

2.3. Free-Energy Calculations. Since bond breaking and forming require the crossing of a relatively large activation barrier, a method to sample the free-energy surface along the relevant reaction coordinate must be employed. In the present study, we applied the technique introduced a few years ago by Parrinello and co-workers.^{53,54} The method is based on a coarse-grained history-dependent dynamics (called metadynamics) that is able to explore the free energy landscape in the space defined by a chosen set of degrees of freedom, $\{\sigma_i\}$ (called collective coordinates), which describe the chemical process. The evolution of the system at every step of the metadynamics is driven by the combined action of the thermodynamic force and a history-dependent force, which penalizes configurations in the collective variable space that have already been visited. The following extended Lagrangian governs the evolution of the system

$$\mathcal{L} = \mathcal{L}^{\text{CP}} + \frac{1}{2} \sum_i M_i \dot{s}_i^2 - \frac{1}{2} \sum_i k_i (\sigma_i - s_i)^2 - V(t, \mathbf{s})$$

where \mathcal{L}^{CP} is the Car–Parrinello Lagrangian; M_i and k_i are the fictitious mass and the coupling constant of the restraints terms, which force the collective variable σ_i to fluctuate around an associated “dynamical” variable s_i (see ref 54 for the details). The history-dependent potential, $V(t, \mathbf{s})$ (with $\mathbf{s} = \{s_i\}$) is constructed as a sum of Gaussians centered on each value of the collective variable previously explored. The potential fills in time the minima of the free energy surface, and as the simulation proceeds, its sum converges to the free energy landscape as a function of the collective variables. It has been demonstrated that meaningful results can be obtained in a relatively short simulation time if the collective variables give a good representation of the initial and final state and include all of the slow modes, which cannot be easily sampled by direct MD.^{53,54}

In the present calculations, atom–atom distances or difference of distances were chosen as reaction coordinates (see sections 3.2 and 3.4). Gaussians were added every 50 steps of MD dynamics. Their height was tuned according to the curvature of the underlying potential (with lower and upper bounds of 0.3 and 42 kJ/mol, respectively), while their width was set to 0.1 Å. The fictitious mass and the coupling constant of the restraints was set to 50 amu and 1 (kJ/mol/Å²), respectively.

3. Results and Discussion

3.1. Protonation State of the Active Site. Knowledge of the protonation state is a prerequisite for modeling the enzymatic reaction. Here we performed geometry minimizations and CP/MM simulations on the protonation states of the active site reported in Figure 2. The following residues were included in the QM region: the cofactor and His⁴⁹⁶, Arg³⁶⁰, Arg⁴⁹⁰, Lys³⁵³, Ser⁴⁰², W1, and W2 (see Figure 1a). In models b and d, His⁴⁰⁴ was also included in the QM calculation. If not explicitly stated, Lys³⁵³, Arg³⁶⁰ and Arg⁴⁹⁰, and are taken in their protonated form.

Unprotonated Vanadate (Charge −3, Models a and b). Here the axial oxygen receives H-bonds from the two waters in the active site (model a). In the geometry optimization process, Lys³⁵³ transfers one of its amino protons to the nearest vanadate equatorial oxygen. The V–N axial bond lengthens from 2.1 to 2.7 Å with the loss of the bipyramidal trigonal coordination. Inclusion of the vanadate/His⁴⁰⁴ H-bond (where His⁴⁰⁴ is taken both in the protonated form and its Nδ tautomer model b) did not alter this picture. In this case, in addition to the proton transfer from Lys³⁵³, an hydrogen abstraction from His⁴⁰⁴ by the axial oxygen was also observed. Thus, our calculations suggest that this species is unstable, consistent with previous calculations,³⁵ which showed that the complex imidazole/VO₄^{3−} in vacuo is also not stable, and the existence of a protonated axial oxygen proposed is experimentally at pH = 8.²⁴

Monoprotonated Vanadate (charge −2, Models c–e). Three HVO₄^{2−}-containing models of the enzyme were considered. In the first two models, the axial oxydriol group donates a H-bond to a water with (model c) and without (model d) receiving a H-bond from His⁴⁰⁴ (again in its protonated form and the Nδ tautomer were considered). In the third model (model e) the axial oxydriol donates a H-bond to His⁴⁰⁴ (Nε tautomer). Geometry optimization of model c leads to the abstraction of hydrogen from Lys³⁵³ by the equatorial oxygen and from Nδ of His⁴⁰⁴ by the axial −O_aH oxydriol group with the formation of an aquavanadate. The calculated V–O_aH₂ distance of 2.3 Å is considerably longer than the observed V–O_a distance in the X-ray structure (1.9 Å), which suggests that this protonation state may be ruled out. Optimization of model d leads, as before,

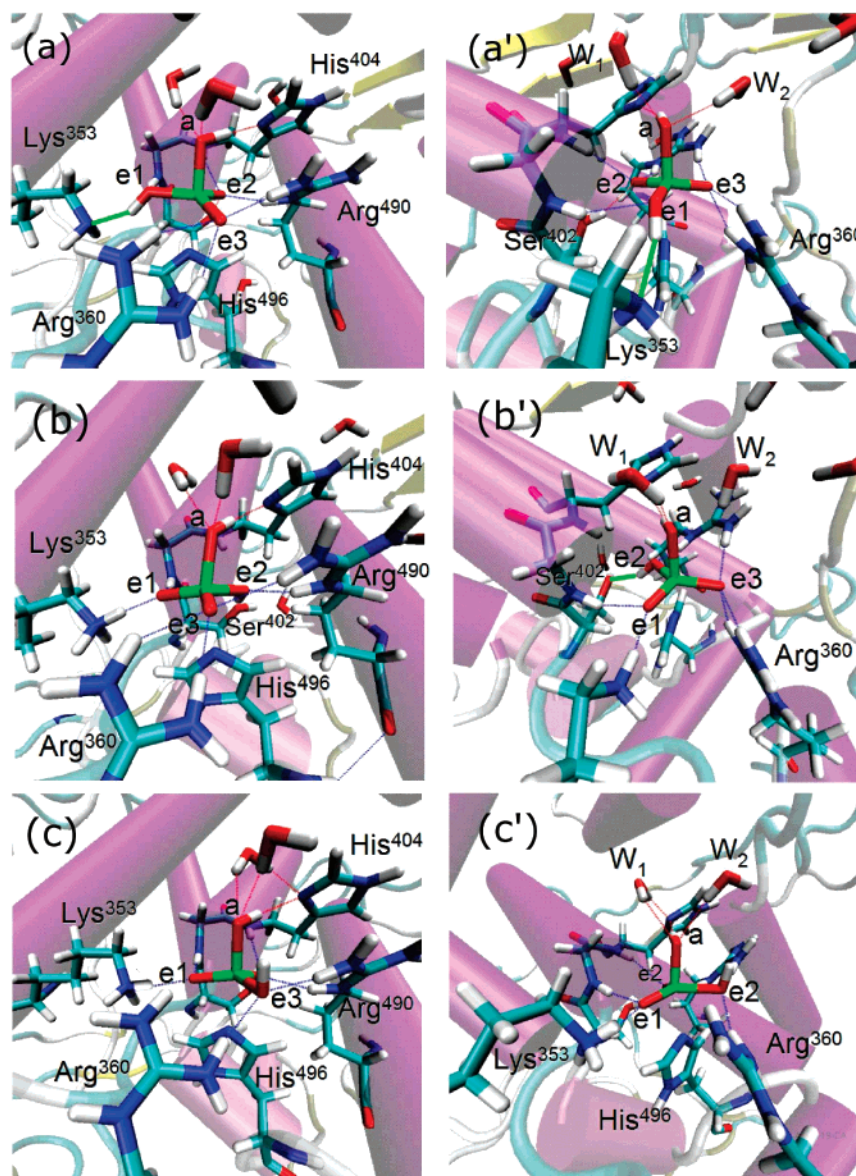


Figure 3. Snapshots of the simulation at 300 K of (a) model e, (b) model f, and (c) model g (see Figure 2). For each protonation state two different views are represented (left and right panels). Selected hydrogen bonds are drawn as dotted lines.

to the deprotonation of Lys³⁵³, but it preserves the bipyramidal trigonal coordination of vanadium. On the other hand, optimization of model e leads to a structure characterized by bipyramidal trigonal coordination and a protonated Lys³⁵³. To access the local stability of model e a short 1 ps molecular dynamics simulation was performed. This resulted in a rapid, ca. 300 fs, hydrogen abstraction from Lys³⁵³ to the equatorial vanadate oxygen. The vanadium coordination appears to be stable on the time scale of the simulation (see Figure 3 and Table 2).

Diprotinated Vanadate (Charge -1, Models f–h). Diprotinated states with one hydrogen on one of the equatorial oxygens (model f to h) were first optimized, and then CP/MM molecular dynamics simulations were performed. In all of these models, the bipyramidal coordination of vanadium was maintained. However, only model f, where O_{e2}–H is H-bonded to, Ser⁴⁰² yields an active site structure in good agreement with the crystallographic one (Figure 3 and Table 2). In the model g, the water W1, is much farther from O_a than in the crystal structure. Furthermore, in this model, the hydrogen bond O_a–H...His⁴⁰⁴ appears to be weakened and the O_{e3}–H group is not able to form an H-bond with the closest water molecule, which cannot access the region near the OH group. However, both

TABLE 2: Average Distances between the Vanadate Moiety and Active Site Residues Calculated at 300 K for Two Different Protonation States of the Enzyme Native State (See Figures 2 and 3)^a

	model e	model f	model g	model h	expt
V–O _a	1.91 (0.05)	1.92 (0.06)	1.90 (0.06)	1.91 (0.05)	1.88
V–O _{e1}	1.75 (0.04)	1.73 (0.02)	1.73 (0.03)	1.77 (0.02)	1.61
V–O _{e2}	1.72 (0.01)	1.91 (0.05)	1.70 (0.02)	1.72 (0.02)	1.63
V–O _{e3}	1.73 (0.01)	1.72 (0.03)	1.96 (0.05)	1.75 (0.04)	1.60
O _a –W ₁	2.76 (0.13)	2.75 (0.12)	3.72 (0.23)	3.75 (0.22)	2.62
O _a –W ₂	2.94 (0.20)	2.81 (0.11)	2.98 (0.16)	2.94 (0.14)	2.78
V–N(His ⁴⁹⁶)	2.32 (0.12)	2.29 (0.07)	2.17 (0.09)	2.19 (0.09)	2.19
O _a –N(His ⁴⁰⁴)	2.86 (0.11)	2.86 (0.09)	3.38 (0.21)	3.31 (0.18)	2.93
O _{e1} –N(Lys ³⁵³)	2.77 (0.16)	2.65 (0.08)	2.73 (0.08)	3.70 (0.13)	2.96
O _{e2} –O(Ser ⁴⁰²)	2.76 (0.12)	2.81 (0.10)	2.78 (0.09)	2.79 (0.10)	2.62
O _{e3} –N ₁ (Arg ³⁶⁰)	2.81 (0.27)	2.78 (0.23)	2.75 (0.27)	2.79 (0.29)	2.96
O _{e3} –N ₁ (Arg ⁴⁹⁰)	3.09 (0.18)	3.17 (0.28)	2.85 (0.33)	3.14 (0.26)	3.11

^a Standard deviation from the mean is reported in parentheses. Experimental data are from ref 25.

Arg³⁶⁰ and Arg⁴⁹⁰ are still H-bonded to O_{e3}. If one (or both) of the arginines are considered neutral (with the C=NH nitrogen being the closest to the O_{e3}–H oxygen), then a rapid transfer of the equatorial proton to the arginine nitrogen and a subsequent

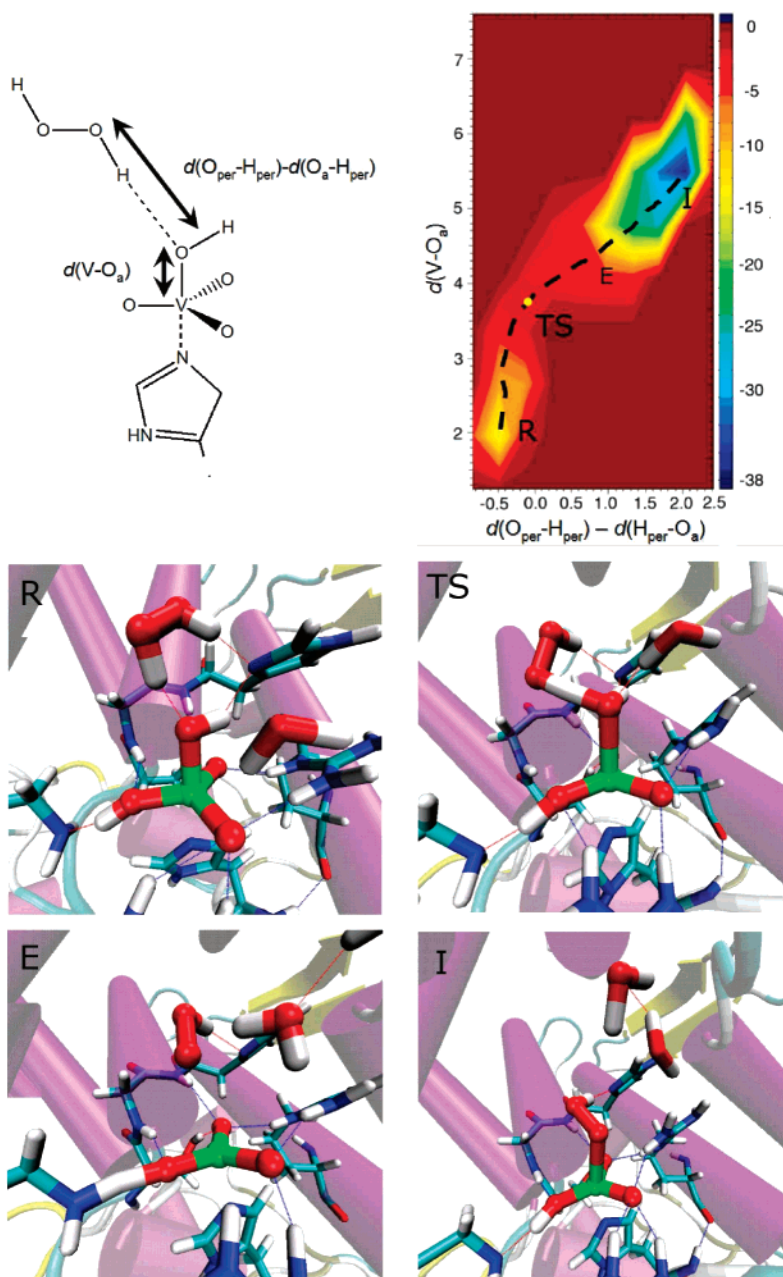


Figure 4. Formation of the hydrogen peroxide intermediate. Upper panels: chosen reactive degrees of freedom (left) and free energy landscape in kJ/mol (right). R: reactants. TS: a configuration near the transition state. E: a configuration after the TS. I: intermediate.

proton transfer from Lys³⁵³ to vanadate were observed. In this case a protonation pattern identical to that of model e is obtained. It is noted that structural optimizations of simple models of the active site, similar to our model f and model g, indicated that both O_{e1} and O_{e3} can be protonated if Lys³⁵³ and Arg³⁶⁰ are, respectively, in a neutral form.³⁵ In model h, if we assume Lys³⁵³ to be protonated, the repulsion between Lys³⁵³ and O_{e1}-H leads to a large distortion of the local geometry. On the other hand, if Lys³⁵³ is assumed neutral, a strong hydrogen bond between the axial oxidril group and Lys³⁵³ is formed, giving rise, again, to a structure similar to model e (Table 2). The only (triprotonated) neutral vanadate moiety we considered (model j) underwent a structural distortion similar to the one observed for models g and h.

To see which model fits best the known catalytic pocket structure, an analysis of the root-mean-square displacement from the crystal structure of the heavy atoms of the vanadate moiety and the residues His⁴⁹⁶, His⁴⁰⁴, Lys³⁵³, Ser⁴⁰², Arg³⁶⁰, Arg⁴⁹⁰,

TABLE 3: Comparison between Stable Protonation States with Root Mean Square Displacement from the Crystal Structure of the Heavy Atoms of the Vanadate Moiety and the Residues His⁴⁹⁶, His⁴⁰⁴, Lys³⁵³, Ser⁴⁰², Arg³⁶⁰, Arg⁴⁹⁰, W1, and W2

model	rmsd (Å)
e	1.1
f	1.5
g	7.4
h	9.7
i	11.8

W1, and W2 was performed (Table 3). Models e and f present the smallest deviation from the crystal structure. Considering in more detail the structure of the vanadate moiety, it is evident that only for model e is the agreement between the calculated and experimental V-O_e fairly good. When O_{e2} and/or O_{e3} are protonated, the V-O_e distance is too long. In this regard, we remark that we have compared the structure of the simulated protein to the crystallographic structure, which actually refers

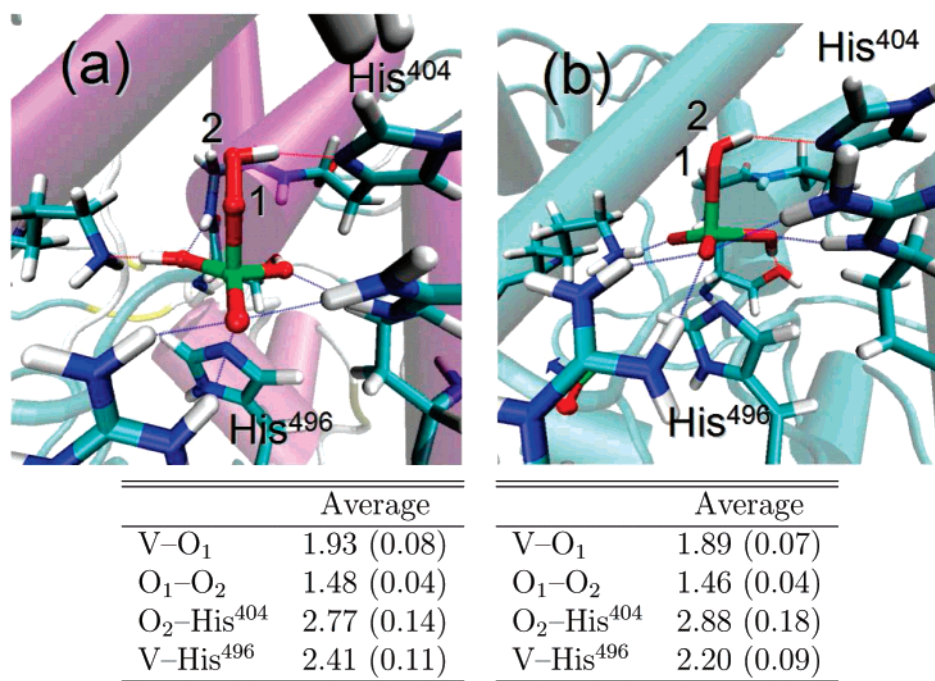


Figure 5. Hydrogen peroxide intermediate species. Average distances between the vanadate moiety and active site residues calculated at 300 K for two different protonation states. Standard deviation from the mean is reported in parentheses. Upper panels: (a) intermediate deriving from model e; (b) intermediate deriving from model f. Selected hydrogen bonds are drawn as dotted lines.

to different thermodynamic conditions (the former is simulated in aqueous solution at neutral pH and room temperature, whereas the latter is packed in a crystal at pH = 8 and low temperature, i.e., 16 °C). Assuming, as is usually done in the simulation of proteins, that aqueous solution and crystal structure do not differ, our conclusions are however fully meaningful.

In summary, the resting state of the enzyme likely consists of an anionic H_2VO_4^- vanadate moiety where one hydroxo is in axial position and H-bonded to His⁴⁰⁴, whereas the other one is either H-bonded to a neutral Lys³⁵³ or to Ser⁴⁰².

We conclude noting that from the analysis of the electronic structure of the $\text{H}_2\text{VO}_4^-/\text{imidazole}$ complex, it is evident that the vanadate moiety is more likely ascribed to a dioxovanadium(V) species (VO_2^+), which strongly interacts with two OH^- anions (see Supporting Information).

3.2. Formation of the Peroxovanadate. We examined the formation mechanism of the peroxo intermediate by hybrid CP/MM simulations for the various possible stable protonation states (models e, f, and g, Figure 2). As reaction coordinates we took the $\text{V}-\text{O}_a$ distance and the asymmetric stretching coordinate defined as $d(\text{O}_{\text{per}} - \text{H}_{\text{per}}) - d(\text{O}_a - \text{H}_{\text{per}})$ (see Figure 4). Here, we explicitly discuss the results obtained for model e in detail, as the other models follow a similar reaction mechanism.

In Figure 4, the free-energy landscape for the O_aH^- attack to the hydrogen peroxide is reported. The reactive path is characterized by the lengthening of the $\text{V}-\text{O}_a$ distance and the increase of the asymmetric stretching coordinate describing the proton transfer from H_2O_2 to O_aH^- (Figure 4). A transition state (TS) is found for $d(\text{V} - \text{O}_a) \approx 3.8 \text{ \AA}$ and $d(\text{O}_{\text{per}} - \text{H}_{\text{per}}) - d(\text{O}_a - \text{H}_{\text{per}}) \approx 0.0 \text{ \AA}$ (Figure 4TS). Once the TS is crossed, a water molecule and a HOO^- anion are formed (Figure 4E). The water molecule diffuses away and, at the same time, the HOO^- anion binds to vanadium with the formation of an hydrogen peroxide intermediate (Figure 4I). This species is stable on the time scale of our simulation (4 ps), and it is obtained starting from *all* of the stable protonation states of the active site. In Figure 5, selected statistical data on distances between atoms

TABLE 4: Activation Free Energy (ΔG^\ddagger) and Reaction Free Energy (ΔG , both in kJ mol^{-1}) for the Formation of the Hydrogen Peroxide Intermediate Starting from Different Protonation States of the Active Site

model	ΔG^\ddagger	ΔG
e	10	28
f	8	33
g	12	30

are reported for two different starting protonation states of the active site. The formation of a hydrogen peroxide intermediate is a nontrivial outcome. So far, its presence has been postulated on the basis of ^{17}O NMR studies of peroxide binding to the active site center of bromoperoxidase from *A. nodosum* at pH = 8.²⁷ An hydrogen peroxide vanadium intermediate has also been suggested in oxo transfer reactions to metal-centered thiulates.^{14,16,55}

The activation free-energy for the formation of the intermediate is quite insensitive to the protonation state of the active site as can be seen from Table 4. In this regard, we remark that the free-energy differences observed among the models are comparable to the statistical error on the free energy itself.⁵⁶ Therefore, we may conclude that different possible protonation states of the enzymes react with hydrogen peroxide following the same reactive route and approximatively the same energetics.

At acidic conditions, the next step of the catalytic cycle reasonably consists of the protonation of the OH oxygen of the hydrogen peroxide group. We investigated this possibility for all of the intermediates by randomly placing a proton at 2–3 Å from the oxygen atom. For every protonation state, starting from different initial geometries, indeed we observed the spontaneous formation of a peroxo species, where the peroxo moiety is hydrogen bonded to Lys³⁵³.

In summary, our calculations suggest that at neutral pH the formation of the peroxo intermediate proceeds through the mechanism reported in Figure 6a, which involves the formation of an (end-on) hydrogen peroxide intermediate. This mechanism differs from that proposed by Messerschmidt et al.,²⁵ which

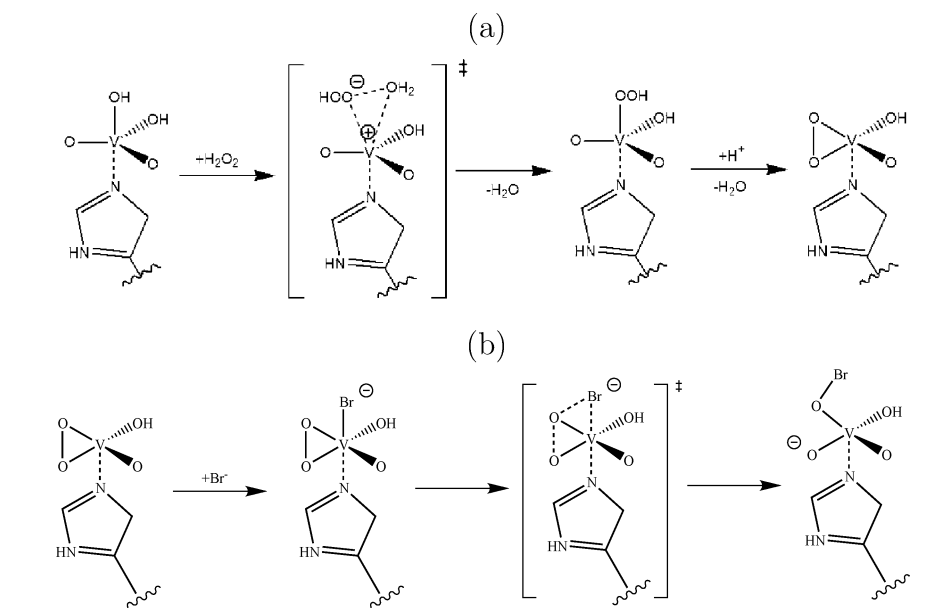


Figure 6. Proposed reaction mechanism for the formation of the peroxovanadate cofactor (a) and the formation of the hypohalogen vanadate intermediate (b).

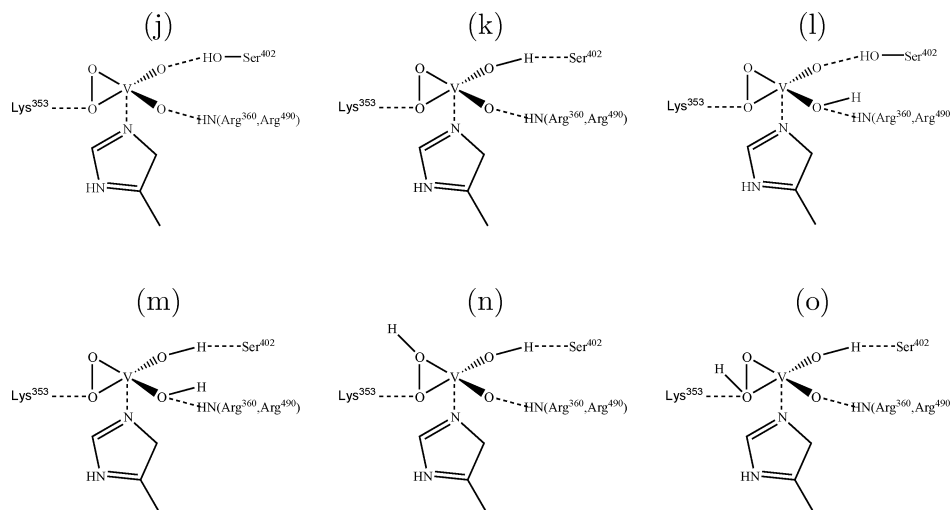


Figure 7. Peroxovanadate protonation states and H-bonding patterns examined.

involves the formation of an aquavanadate species and the release of HOO^- that in turns attacks the vanadium center with the subsequent formation of the peroxo species. On the basis of our calculations, the HOO^- is too reactive and the water is very weakly bound to vanadium (see also ref 35) to have an appreciable lifetime, especially at acidic conditions. In this regard the mechanism found in our study, which involves a quasi-concerted H_2O_2 deprotonation/water release with the formation of the hydrogen peroxide intermediate, seems to be more realistic. It must be also noted that our results suggest that, at low pH, the hydrogen peroxide intermediate has probably a very short (maybe not detectable) lifetime.

3.3. Protonation State of the Peroxovanadate. After its formation the peroxovanadate cofactor can undergo several protonation equilibria. As done for the ground state of the enzyme, we have determined the most probable protonation state comparing CP/MM calculations to the crystal structure. In Figure 7, the protonation states of the peroxovanadate cofactor considered in this study are reported. The following residues were included in the QM region: the cofactor and His⁴⁹⁶, Arg³⁶⁰, Arg⁴⁹⁰, Lys³⁵³, Ser⁴⁰², and a water molecule. Again, if not

explicitly stated, Lys³⁵³, Arg³⁶⁰, and Arg⁴⁹⁰ are taken in their protonated form.

Water Binding. All of the structures obtained from our simulations are characterized by a water molecule weakly coordinated to the metal (Figure 8 and Table 5). In the crystallographic structure, no water is reported in that position (the nearest water is at about 4.4 Å from the metal center; see Figure 1b). This molecule diffuses close to vanadium during the classical MD, because of the large empty space existing in the experimentally determined structure, and it remains stably bound during the entire CP/MM simulation. The average $\text{V}-\text{O}_{\text{wat}}$ distance ranges from about 3.0 Å in model j to 2.6 Å in the other models. In the simulations, the water network between the active site and the solution considerably rearranges, but, at equilibrium, almost all of the occupancies of the crystallographic positions are recovered. In model k, if we constrain the water molecule–vanadium distance to the experimental value in order to prevent the coordination with vanadium, a significantly longer $\text{V}-\text{N}_{\text{e}}(\text{His}^{496})$ is obtained (2.31 instead of 2.07 Å). This finding suggests that a water molecule

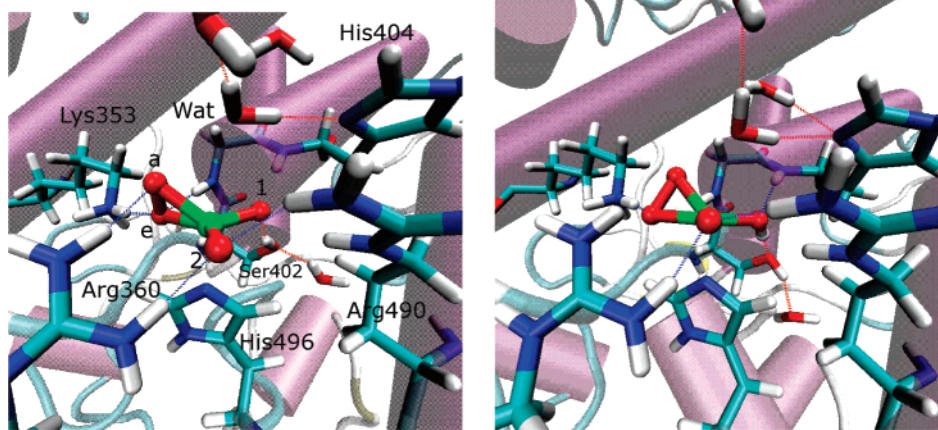


Figure 8. Snapshots of the simulation at 300 K of (a) model j and (b) model k of the peroxovanadate containing enzyme (see Figure 7). Selected hydrogen bonds are drawn as dotted lines.

TABLE 5: Average Distances between the Peroxovanadate Moiety and Active Site Residues Calculated at 300 K for Different Protonation States of the Peroxo Cofactor (See Figures 7 and 8)^a

	model j	model k	model l	model m	expt
V–O ₁	1.72 (0.02)	1.80 (0.02)	1.68 (0.01)	1.81 (0.01)	1.61
V–O ₂	1.71 (0.01)	1.69 (0.02)	1.91 (0.01)	1.86 (0.01)	1.93
V–O _a	1.89 (0.03)	1.88 (0.04)	1.89 (0.04)	1.83 (0.04)	1.89
V–O _e	1.87 (0.04)	1.89 (0.03)	1.89 (0.03)	1.84 (0.03)	1.86
O _a –O _e	1.48 (0.02)	1.47 (0.02)	1.48 (0.02)	1.48 (0.02)	1.47
O ₁ –O(Ser ⁴⁰²)	2.92 (0.13)	2.76 (0.11)	2.92 (0.13)	2.89 (0.11)	2.90
O ₂ –N ₁ (Arg ³⁶⁰)	2.80 (0.12)	2.96 (0.10)	2.95 (0.11)	3.61 (0.16)	3.03
O _a –N _ε (Lys ³⁵³)	2.79 (0.18)	2.82 (0.13)	2.79 (0.18)	4.02 (0.21)	2.67
V–O _{Wat}	2.96 (0.21)	2.63 (0.16)	2.62 (0.11)	2.58 (0.10)	(4.39)
V–N _ε (His ⁴⁹⁶)	2.10 (0.03)	2.07 (0.04)	2.08 (0.03)	2.11 (0.03)	2.19
RMSD	5.4	1.8	1.4	10.1	-

^a Standard deviation from the mean is reported in parentheses. In the last row, the root mean-square displacement (rmsd) from the crystal structure of the heavy atoms of the vanadate moiety and the residues His⁴⁹⁶, His⁴⁰⁴, Lys³⁵³, Ser⁴⁰², Arg³⁶⁰, Arg⁴⁹⁰, W1, and W2 is also reported. Experimental data are from ref 25.

coordinated to vanadium might be important for the stability of the cofactor/histidine complex.

Protonated Peroxo Oxygen Species (Charge 0, Models n and o). The species protonated on the peroxo oxygens (model n and o) are not stable or give rise to large distortions of the catalytic pocket with respect to crystallographic structure. This conclusion seems to be independent of the protonation state of the oxo oxygens. For the cases where Lys³⁵³ is charged, model n releases the pseudoaxial proton to the nearby water molecule, whereas in model o the N_ε–O_e distance lengthens to 4.3 Å (experimental 2.67 Å²⁵). On one hand, when Lys³⁵³ is not protonated, both in model n and model o, the peroxo proton is promptly transferred to the lysine N_ε.

Diprotonated Oxo Oxygen Species (Charge +1, Model m). The peroxo form with two equatorial hydroxyl groups (model m) undergoes large distortions with respect to the crystal structure (Table 5). If Lys³⁵³ is charged, the H-bonds between the peroxo moiety and both Lys³⁵³ and Arg³⁶⁰ are lost. The calculated average O_a–N_ε(Lys³⁵³) and O₂–N₁(Arg³⁶⁰) are 4.02 and 3.61 Å, respectively, whereas the experimental values are 2.67 and 3.03 Å. If Lys³⁵³ and/or Arg³⁶⁰ are not protonated the agreement with the crystal structure improves, but O_a–N_ε–(Lys³⁵³) and O₂–N₁(Arg³⁶⁰) distances are still too long (respectively, about 3.3 and 3.2 Å).

Unprotonated and Monoprotonated Oxo Species (Charge –1 and 0, Models j, k, and l). The anionic form (model j) and the neutral states with an equatorial oxidril group (models

k and l) appear to be stable. Statistical data on distances between atoms in the active site are given in Table 5 (see also Figure 8). Among the different peroxo species, model l has structural features of the active site in good agreement with the X-ray data²⁵ (in terms of V–O distances and H-bonds distances between the peroxo moiety and the active site residues). This species is characterized by the presence of an unprotonated peroxo group, one oxo oxygen, and one hydroxo group, which forms a weak hydrogen bond with a water molecule in the active site. Nevertheless, on the base of the root-mean-square displacement with respect to the crystal structure also model k shows a good agreement with experiment (Table 5).

3.4. Halide Binding and Reactivity. The last step of our investigation is the study of the bromide anion binding to the peroxovanadate cofactor and the subsequent oxo transfer pathway. Different protonation states were considered: unprotonated (anionic, model j), singly oxo-protonated (neutral, model k, and l), and diprotonated (positively charged, model m) cofactors.

The binding of Br[–] was studied by performing CP/MM simulations where the coordination water was removed and the anion was randomly placed at 4 Å from the metal center. For the neutral and positively charged species, a spontaneous binding of bromide was observed (Figure 9). Selected statistical data on distances are reported in Table 6. All of the adducts are characterized by an average V–Br distance at 300 K of about 2.6 Å and a Br–O_a distance of about 3.0 Å. In contrast to what was reported for model m in section 3.3, in the adduct formed by model m, Lys³⁵³ and Arg³⁶⁰ are H-bonded to the peroxo-vanadate moiety (Table 6). The anionic form does not spontaneously bind the halogen, as expected for a reaction between two negatively charged substrates. Furthermore, in model j, starting from an initial V–Br distance of 2.6 Å, the halogen was immediately repelled by the cofactor. This is clearly a consequence of the fact (i) that the V–Br interaction is relatively weak (as indicated by the average V–Br distance) and (ii) that the negative charge delocalized on the oxo oxygens of the cofactor, which is not “compensated” by the positive charges on the coordinating Arg³⁶⁰ and Arg⁴⁹⁰, prevents a stable binding.

On the other hand, all of the attempts to find a reaction path for the direct binding of Br[–] to O_a failed for all of the protonation states. These findings strongly suggest that a binding of the halogen to vanadium prior oxidation may take place, as also suggested by a steady-state kinetic analysis on bromoperoxidases.³² Previous calculations by Zampella et al.³⁶ also support this proposal. We observe in passing that, upon halogen

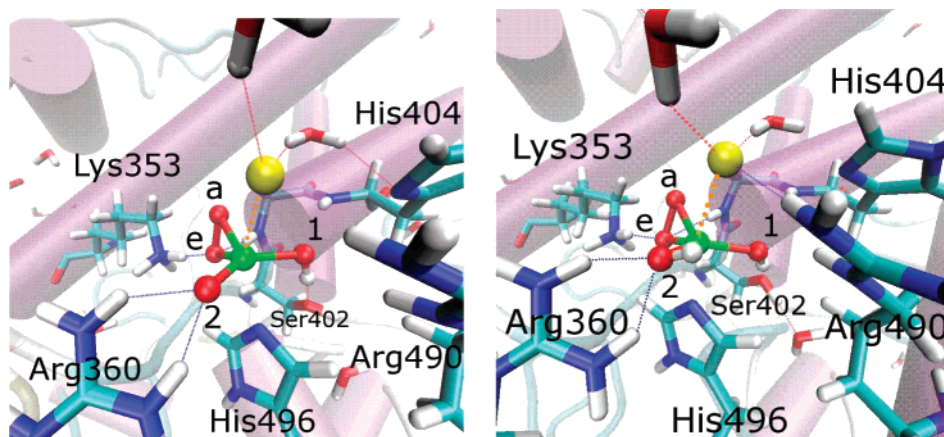


Figure 9. Snapshots of the simulation at 300 K of the peroxovanadate/ Br^- adduct obtained for different protonation states of the peroxo moiety: (a) model k and (b) model m (see Table 6). Selected hydrogen bonds are drawn as dotted lines.

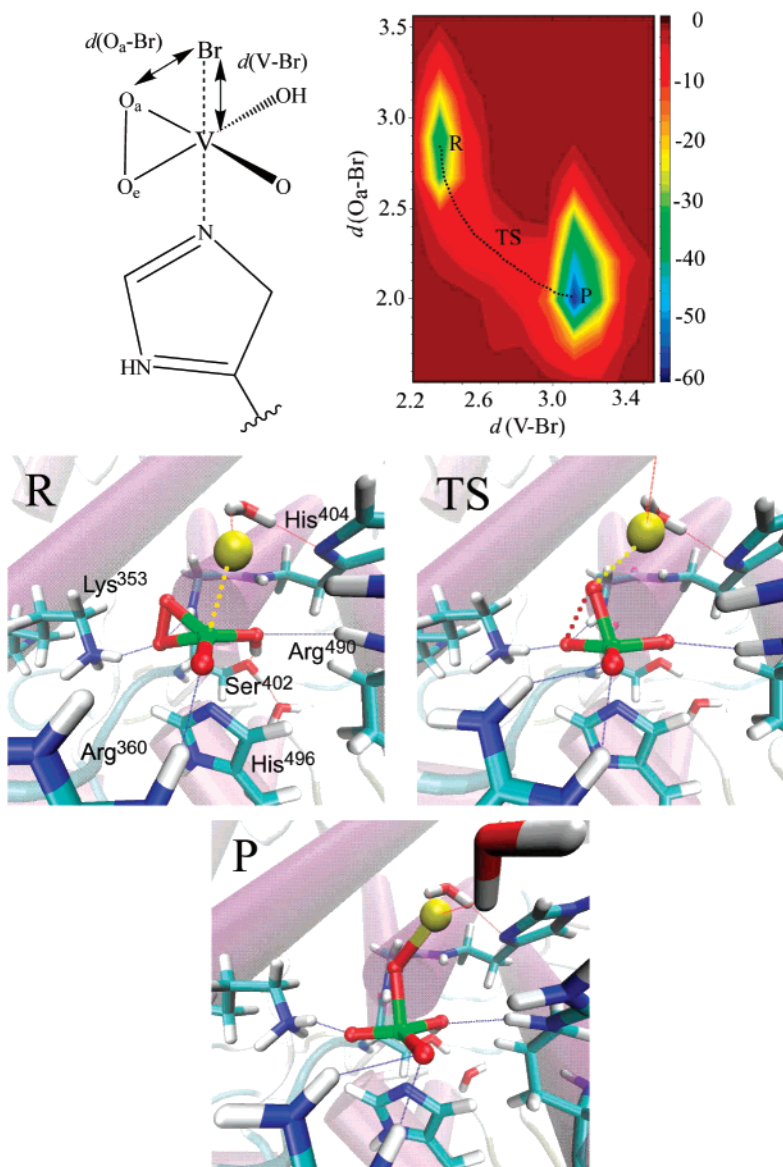


Figure 10. Initial stage of bromide anion oxidation. Upper panels: chosen reactive coordinates (left) and free energy landscape in kJ/mol (right). R: reactants. TS: a configuration near the transition state. P: final state.

binding all of the V–O distances slightly increase, whereas the peroxo O–O distance decrease. More remarkably, the adduct shows a considerably shorter (0.10–0.15 Å) H-bond with Lys³⁵³ (Table 6).

Taking as reaction coordinate the V–Br and O_a –Br distances, a pathway leading to the oxo transfer to the Br is found. Some snapshots of this process and the relative free-energy landscape for model k are reported in Figure 10. Similar pathways are

TABLE 6: Average Distances between the Peroxovanadate/Br Adduct and Active Site Residues Calculated at 300 K for Different Protonation States of the Peroxo Moiety (See Figure 9)^a

	model k	model l	model m
V–O ₁	1.86 (0.02)	1.76 (0.01)	1.86 (0.02)
V–O ₂	1.71 (0.02)	1.98 (0.02)	1.91 (0.02)
V–O _a	1.91 (0.03)	1.92 (0.02)	1.88 (0.04)
V–O _e	1.92 (0.03)	1.93 (0.03)	1.89 (0.03)
O _a –O _e	1.45 (0.03)	1.46 (0.02)	1.46 (0.02)
O ₁ –O(Ser ⁴⁰²)	2.89 (0.12)	2.99 (0.16)	2.96 (0.11)
O ₂ –N ₁ (Arg ³⁶⁰)	2.83 (0.10)	2.85 (0.11)	2.91 (0.16)
O _a –N ₅ (Lys ³⁵³)	2.64 (0.11)	2.63 (0.13)	2.72 (0.15)
V–Br	2.56 (0.12)	2.57 (0.13)	2.61 (0.11)
V–N _ε (His ⁴⁹⁶)	2.15 (0.05)	2.17 (0.04)	2.19 (0.04)

^a Standard deviation from the mean is reported in parentheses.

TABLE 7: Activation Free Energy (ΔG^\ddagger) and Reaction Free Energy (ΔG , Both in kJ mol^{−1}) for the Oxidation of Br[−] Starting from Different Peroxovanadate/Br[−] Adducts

model	ΔG^\ddagger	ΔG
k	24	20
l	28	26
m	35	24

found for the other peroxovanadate/Br[−] adducts. In Table 7 a summary of the reaction energetics is reported. The difference in the activation free-energy between model k and model l is quite small and within our statistical uncertainty.⁵⁶ Hence, our calculations cannot discriminate between the two different protonation states, even though model k seems to present the lowest activation barrier, in agreement with the experimental evidence.^{1,15,24} For model k, we have also studied the reaction assuming Lys³⁵³ as neutral. In this case, the activation free-energy increases to 32 kJ/mol. This effect of the protonation state of Lys³⁵³ was already pointed out by Zampella et al.³⁶ Here we confirm that LysH⁺ polarizes the O–O peroxo bond and, as a consequence, lowers the activation energy for oxo transfer. The RESP charge difference, Δq , on the peroxo atoms is $\Delta q(\text{O}_a-\text{O}_e) = 0.11 e$ when Lys³⁵³ is charged and 0.01 e when it is neutral. The N_ε–H⁺···O_e H-bond is very strong all along the reaction path ($1.5 \text{ \AA} < d(\text{H} \cdots \text{O}_e) < 1.7 \text{ \AA}$). During the formation of the hypohalogen vanadate, however no proton-transfer attempts from Lys³⁵³ to O_e were observed. The reaction mechanism for the initial stage of the halogen oxidation is reported in Figure 6b.

4. Conclusion

In this paper, we have reported a structural analysis of the resting state of the vanadium dependent chloroperoxidase and a study of the early intermediates of the catalytic cycle. The main results obtained on the initial stages of the catalytic activity are reported in Figure 6. The investigation of different protonation states indicates that the rest enzyme likely consists of an anionic H₂VO₄[−] vanadate moiety where one hydroxo is in axial position and H-bonded to His⁴⁰⁴. The comparison with the crystal structure suggests that the second hydroxo group is either H-bonded to a neutral Lys³⁵³ or to Ser⁴⁰². In all likelihood, depending on the pH, several different protonation states can coexist. Our calculations suggest that the hydrogen peroxide addition may not involve an initial protonation of the cofactor in contrast to previous proposals.³ We found a low free energy barrier path where the hydrogen peroxide directly attacks the axial hydroxo group with the formation of an hydrogen peroxide intermediate, which is promptly protonated in acidic conditions

to form a peroxo species. Furthermore, the free energy barrier for the formation of the hydroperoxide intermediate does not depend significantly upon the protonation state of the cofactor. The most probable protonation states of the peroxo cofactor are neutral HVO₂(O₂) forms with hydroxo group either H-bonded to Ser⁴⁰² (model k) or coordinated to Arg³⁶⁰ (model l). The peroxo cofactor is also coordinated to an axial water molecule, which is likely important for the stability of the peroxovanadate/His⁴⁹⁶ adduct. Our calculations do not support the protonation of one of the two peroxo oxygen as initial step of the halide oxidation. Instead, the halogen first displaces the axial water and coordinates to vanadium and then reacts with the peroxo moiety yielding a hypohalogen vanadate. The most reactive protonation state of peroxovanadate is the neutral HVO₂-(O₂) with the hydroxo group H-bonded to Ser⁴⁰² (model k). Further studies are deemed necessary to investigate the possibility that the hypohalogen vanadate intermediate is actually stable and therefore has an appreciable lifetime.⁴ We also confirm that a protonated Lys³⁵³ could play a crucial role determining the catalytic activity, strongly polarizing the peroxo moiety. It has been also proposed that perturbation induced by Lys³⁵³ is possibly an important factor for tuning the reactivity of the enzyme toward Cl[−] and Br[−].³⁶ From our calculations, however, no evidence of a proton transfer to the peroxo group is observed during the formation of the hypohalogen intermediate. On the contrary, a protonated peroxo moiety, which has been proposed to participate in the reaction,¹⁵ turns out to be extremely unstable and therefore is not likely involved in the catalytic cycle.

Acknowledgment. We are grateful to the MURST Cofin for financial support and to the INFN/CINECA for a large computer grant. We thank Dr. R. Rousseau for many stimulating discussions.

Supporting Information Available: Figure SI, showing electron density isosurfaces of the H₂VO₄/pyrrole complex and text describing the calculations. This material is available free of charge via the Internet at <http://pubs.acs.org>.

References and Notes

- (1) Rehder, D. *Coord. Chem. Rev.* **1999**, 182, 297–322.
- (2) Butler, A. *Science* **1998**, 281, 207–210.
- (3) Crans, D. C.; Smee, J. J.; Gaidamauskas, E.; Yang, L. *Chem. Rev.* **2004**, 104, 849–902.
- (4) Butler, A. *Coord. Chem. Rev.* **1999**, 187, 17–35.
- (5) Littlechild, J. *Curr. Opin. Chem. Biol.* **1999**, 3, 28–34.
- (6) Ligtenbarg, G. J. A.; Hage, R.; Feringa, B. L. *Coord. Chem. Rev.* **2003**, 237, 89–101.
- (7) Chen, J.; Christiansen, J.; Tittsworth, R. C.; Hales, B. J.; George, S. J.; Coucouvanis, D.; Cramer, S. P. *J. Am. Chem. Soc.* **1993**, 115, 5509–5515.
- (8) Eady, R. R. *Coord. Chem. Rev.* **2003**, 237, 23–30.
- (9) Butler, A. *Curr. Opin. Chem. Biol.* **1998**, 2, 279–285.
- (10) Butler, A.; Clague, M. J.; Meister, G. E. *Chem. Rev.* **1994**, 94, 625–638.
- (11) Rehder, D.; Santoni, G.; Licini, G. M.; Schulzke, C.; Meier, B. *Coord. Chem. Rev.* **2003**, 237, 53–67.
- (12) Pooransingh, N.; Pomerantseva, E.; Ebel, M.; Jantzen, S.; Rehder, D.; Polenova, T. *Inorg. Chem.* **2003**, 42, 1256–1266.
- (13) Zhang, X.; Meuwly, M.; Woggon, W.-D. *J. Inorg. Biochem.* **2004**, 98, 1967–1970.
- (14) Smith, T. S.; Pecoraro, V. L. *Inorg. Chem.* **2002**, 41, 6754–6760.
- (15) Colpas, G. J.; Hamstra, B. J.; Kampf, J. W.; Pecoraro, V. L. *J. Am. Chem. Soc.* **1996**, 118, 3469–3478.
- (16) Hamstra, B. J.; Colpas, G. J.; Pecoraro, V. L. *Inorg. Chem.* **1998**, 37, 949–955.

- (17) Sheldon, R. A.; Kochi, J. K. *Metal-Catalyzed Oxidations of Organic Compounds*; Academic Press: New York, 1981.
- (18) Mimoun, H.; Saussine, L.; Daire, E.; Postel, M.; Fischer, J.; Weiss, R. *J. Am. Chem. Soc.* **1983**, *105*, 3101–3110.
- (19) Conte, V.; Furia, F. D.; Moro, S. *J. Phys. Org. Chem.* **1996**, *9*, 329–336.
- (20) ten Brink, H. B.; Tuyman, A.; Dekker, H. L.; Hemrika, W.; Izumi, Y.; Oshiro, T.; Schoemaker, H. E.; Wever, R. *Inorg. Chem.* **1998**, *37*, 6780–6784.
- (21) ten Brink, H. B.; Holland, H. L.; Schoemaker, H. E.; van Lingem, H.; Wever, R. *Tetrahedron: Asymmetry* **1999**, *10*, 4563–4572.
- (22) Weyand, M.; Hecht, H. J.; Kiess, M.; Liaud, M. F.; Vilter, G.; Schomburg, D. *J. Mol. Biol.* **1999**, *293*, 595–611.
- (23) Isupov, M. I.; Dalby, A. R.; Brindley, A. A.; Izumi, Y.; Tanabe, T.; Murshudov, G. N.; Littlechild, J. A. *J. Mol. Biol.* **2000**, *299*, 1035–1049.
- (24) Messerschmidt, A.; Wever, R. *Proc. Natl. Acad. Sci. U.S.A.* **1996**, *93*, 392–396.
- (25) Messerschmidt, A.; Prade, L.; Wever, R. *Biol. Chem.* **1997**, *378*, 309–315.
- (26) Messerschmidt, A.; Wever, R. *Inorg. Chim. Acta* **1998**, *273*, 160–166.
- (27) Casny, M.; Rehder, D.; Schmidt, H.; Vilter, H.; Conte, V. *J. Inorg. Biochem.* **2000**, *80*, 157–160.
- (28) Plass, W. *Coord. Chem. Rev.* **2003**, *237*, 205–212.
- (29) Ohshiro, T.; Littlechild, J.; Garcia-Rodriguez, E.; Isupov, M. N.; Ida, Y.; Kobayashi, T.; Izumi, Y. *Protein Sci.* **2004**, *13*, 1566–1571.
- (30) Soedjak, H.; Walker, J. V.; Butler, A. *Biochemistry* **1995**, *34*, 12689–12696.
- (31) Everett, R. R.; Soedjak, H. S.; Butler, A. *J. Biol. Chem.* **1990**, *265*, 15671–15679.
- (32) de Boer, E.; Wever, R. *J. Biol. Chem.* **1988**, *263*, 12326–12332.
- (33) Borowski, T.; Szczepanik, W.; Chruszcz, M.; Broclawik, E. *Int. J. Quantum Chem.* **2004**, *99*, 864–875.
- (34) Balcells, D.; Maseras, F.; Lledós, A. *J. Org. Chem.* **2003**, *68*, 4265–4274.
- (35) Zampella, G.; Kravitz, J. Y.; Webster, C. E.; Fantucci, P.; Hall, M. B.; Carlson, H. A.; Pecoraro, W. L.; Gioia, L. D. *Inorg. Chem.* **2004**, *43*, 4127–4136.
- (36) Zampella, G.; Fantucci, P.; Pecoraro, V. L.; Gioia, L. D. *J. Am. Chem. Soc.* **2005**, *127*, 953–960.
- (37) Buhl, M.; Schurhammer, R.; Imhof, P. *J. Am. Chem. Soc.* **2004**, *126*, 3310–3320.
- (38) (a) Car, R.; Parrinello, M. *Phys. Rev. Lett.* **1985**, *55*, 2471–2474.
(b) Marx, D.; Hutter, J. In *Modern Methods and algorithms of quantum chemistry*; Grotendorst, J., Ed.; NIC Series 1; John von Neumann Institute for Computing: Jülich, Germany, 2000; pp 301–349.
- (39) Laio, A.; VandeVondele, J.; Rothlisberger, U. *J. Chem. Phys.* **2002**, *116*, 6941–6947.
- (40) Laio, A.; VandeVondele, J.; Rothlisberger, U. *J. Phys. Chem. B* **2002**, *106*, 7300–7307.
- (41) Bermanand, H. M.; Westbrookand, J.; Fengand, Z.; Gillilandand, G.; Bhatand, T. N.; Weissigand, H.; Shindyalovand, I. N.; Bourne, P. E. *Nucleic Acids Res.* **2000**, *28*, 235–242.
- (42) Case, D.; Pearlman, D.; Caldwell, J.; III, T. C.; Wang, J.; Ross, W.; Simmerling, C.; Darden, T.; Merz, K.; Stanton, R.; Cheng, A.; Vincent, J.; Crowley, M.; Tsui, V.; Gohlke, H.; Radmer, R.; Duan, Y.; Pitera, J.; Massova, I.; Seibel, G.; Singh, U.; Weiner, P.; Kollman, P. Amber7 Technical report: University of California: San Francisco, CA, 2002.
- (43) Chiba, H.; Nishidate, K.; Baba, M.; Kumagai, N.; Sato, T.; Nishikawa, K. *Solid State Commun.* **1999**, *110*, 497–502.
- (44) Sherwood, P. In *Modern Methods and Algorithms of Quantum Chemistry Proceedings*; Grotendorst, J., Ed.; NIC Series 3; John von Neumann Institute for Computing: Jülich, Germany, 2000; pp 285–305.
- (45) Hutter, J.; Alavi, A.; Deutch, T.; Bernasconi, M.; Goedecker, S.; Marx, D.; Tuckerman, M.; Parrinello, M. CPMD. MPI für Festkörperforschung und IBM Zurich Research Laboratory, Zurich, Switzerland, 1995–1999.
- (46) Hamprecht, F. A.; Cohen, A. J.; Tozer, D. J.; Handy, N. C. *J. Chem. Phys.* **1998**, *109*, 6264–6271.
- (47) Parthiban, S.; de Oliveira, G.; Martin, J. M. L. *J. Phys. Chem. B* **2001**, *105*, 895–904.
- (48) Raugei, S.; Cardini, G.; Schettino, V. *J. Chem. Phys.* **2001**, *114*, 4089–4098.
- (49) Raugei, S.; Klein, M. L. *J. Phys. Chem. B* **2001**, *105*, 8212–8219.
- (50) Troullier, N.; Martins, J. L. *Phys. Rev. B* **1991**, *43*, 1993–2006.
- (51) See, e.g.: Sprik, M.; Hutter, J.; Parrinello, M. *J. Chem. Phys.* **1996**, *105*, 1142. Giannozzi, P. In *Computational Approaches to Novel Condensed Matter Systems, Proceedings of 3rd Gordon Godfrey Workshop on Condensed Physics*; Neilson, D., Das, M. P., Eds.; Plenum: New York, 1995.
- (52) Apra, E.; Windus, T. L.; Straatsma, T. P.; Bylaska, E. J.; de Jong, W.; Hirata, S.; Valiev, M.; Hackler, M. T.; Pollack, L.; Kowalski, K.; Harrison, R. J.; Dupuis, M.; Smith, D. M. A.; Nieplocha, J.; Tipparaju, V.; Krishnan, M.; Auer, A. A.; Brown, E.; Cisneros, G.; Fann, G. I.; Fruchtl, H.; Garza, J.; Hirao, K.; Kendall, R.; Nichols, J. A.; Tsemekhman, K.; Wolinski, K.; Anchell, J.; Bernholdt, D.; Borowski, P.; Clark, T.; Clerc, D.; Dachselt, H.; Deegan, M.; Dyall, K.; Elwood, D.; Glendenning, E.; Gutowski, M.; Hess, A.; Jaffe, J.; Johnson, B.; Ju, J.; Kobayashi, R.; Kutteh, R.; Lin, Z.; Littlefield, R.; Long, X.; Meng, B.; Nakajima, T.; Niu, S.; Rosing, M.; Sandrone, G.; Stave, M.; Taylor, H.; Thomas, G.; van Lenthe, J.; Wong, A.; Zhang, Z. NWChem, A Computational Chemistry Package for Parallel Computers, Version 4.7; Pacific Northwest National Laboratory: Richland, WA, 2005.
- (53) Laio, A.; Parrinello, M. *PNAS* **2002**, *99*, 12562–12566.
- (54) Iannuzzi, M.; Laio, A.; Parrinello, M. *Phys. Rev. Lett.* **2003**, *90*, 238302.
- (55) Ghiron, A. F.; Thompson, R. C. *Inorg. Chem.* **1990**, *29*, 4457–4461.
- (56) Laio, A.; Rodriguez-Fortea, A.; Gervasio, F. L.; Ceccarelli, M.; Parrinello, M. *J. Phys. Chem. B* **2005**, *109*, 6714–6721.